



Influence of promoted bimetallic Ni-based catalysts and Micro/Mesopores carbonaceous supports for biomass hydrothermal conversion to H₂-rich gas

Mohammad Salimi, Ahmad Tavasoli*, Salar Balou, Havva Hashemi, Komeil Kohansal

School of Chemistry, College of Science, University of Tehran, Tehran, Iran



ARTICLE INFO

Keywords:

Hydrothermal gasification
Hydrothermal carbonization
Graphene nano sheets
Activated carbon
Agricultural wastes
Ni catalysts
Hydrogen

ABSTRACT

We report herein, a green route of energy generation from lignocellulosic wastes, the production of H₂ from catalytic hydrothermal gasification of Iranian canola stalks (CS). Firstly, we performed the non-catalytic tests in a stainless-steel batch micro reactor to determine the impacts of operational parameters (temperature, time and feedstock concentration) and optimize them. The achieved optimized control factors were found to be 440 °C and 20 min, and 2.5 wt% for temperature, reaction time, and feed concentration, respectively. Furthermore, the optimum control factors were used to examine the impacts of Ni catalysts supported on two different supports (activated carbon (AC) and Graphene Nano sheets (GNS)) on the mole fractions and yields of H₂ in details. Hence, we investigated the impacts of novel bimetallic catalysts, (Ni-Ru, Ni-Co, and Ni-Cu) supported on GNS for the first time and the optimized catalyst promoter was also impregnated separately on AC to improve and achieve the highest H₂ yield possible. Among the prepared catalysts, the Ni-Cu/AC catalyst showed the best performance with the highest H₂ gas yield and lowest methane production of 20.96 and 2.19 (mmolgas. g_{CS}⁻¹), respectively. H₂ gas production was monitored during the HTG process using gas chromatography and the physiochemical properties of the prepared catalysts were also examined by various techniques.

1. Introduction

In recent decades, an overdependence on fossil fuels has heightened serious environmental problems such as greenhouse effect, and air pollution [1]. Moreover, a future without fossil fuels is not unexpected as these depleting resources are not infinite and their natural replenishment takes a very long time [2]. Finding a clean and non-limited alternative energy source which is renewable can help us shape a green future by resolving the mentioned difficulties [3]. Energy generation from renewable resources, especially biomass, is more difficult than fossil fuels because such resources need an intermediate step of conversion to make usable energy [4]. Nevertheless, deriving energy from renewable biomass produces near zero pollution during the process which is a priority for achieving energy and environmental sustainability [5].

Lignocellulosic biomass as an example of widely distributed and renewable energy source with a high content of cellulose in their structures is very susceptible for fuel gases generation [6]. The high productivity of lignocellulosic biomass in Mazandaran (the northern state of Iran) with annual production of 30 million tons of canola, rice, and barley (major crops) provides a huge source of waste materials (after harvesting) which could be a promising resource for energy

generation through thermal, chemical and thermochemical conversion routes [7]. Among these technologies, HTG have several advantages such as lack of feedstock drying step, absence of mass transfer limitation due to the unique properties of SCW as a non-polar solvent, better product separation due to the drastic change in water properties from non-polar solvent to polar by a small change in operating condition, moderate operating temperature and etc. In contrast to these advantageous, some technical barriers like high pressure environment and consequently some safety problems slow down the process development and scale up to industrial scale. By the way, in a recent work presented by the Tushar et.al, the catalytic SCW of specific microalgae using 5% Ru/C was performed at 400 °C [8]. What is very promising is that the HTG was carried out non-stop for 100 h at the microalgae production site in Switzerland. The fact that they carried out the HTG process at the biomass production site, shows the feasibility of its scale up and the awaiting superiority of the process and carbon supported catalysts over other techniques of biomass conversions such as steam gasification, pyrolysis, and reforming [9]. These results might be an encouraging sign for the upcoming researchers and industries to replace the older techniques with the HTG process [10].

Lignocellulose forms a complex network in plant cell wall that holds them together by covalent bonds, intermolecular hydrogen bonds, and

* Corresponding author.

E-mail address: tavasoli.a@ut.ac.ir (A. Tavasoli).

Nomenclature		ICP-AES	Inductively Spectroscopy	Coupled	Plasma	Atomic	Emission
Abbreviations		ICP-OES	Inductively Spectrometry	Coupled	Plasma-Optical	Emission	
AC	Activated carbon	PSD	Pore size distributions				
BET	Brunauer–Emmett–Teller	SCW	Supercritical water				
CS	Canola stalk	TPR	Temperature-programmed reduction				
CCE	Carbon conversion efficiency	TEM	Transmission Electron Microscopy				
CGE	Carbon gasification efficiency	TOC	Total organic carbon				
CLE	Carbon liquefaction efficiency	TOF	Turnover frequency				
CSE	Carbon solidification efficiency	WGS	Water-gas shift				
CHTG	Catalytic hydrothermal gasification	Wt%	Weight percent				
CVD	Chemical vapor deposition	XRD	X-ray powder diffraction				
FT-IR	Fourier Transform Infrared Spectroscopy						
FESEM	Field Emission Scanning Electron Microscopy						
GC	Gas chromatography						
GNS	Graphene nanosheets						
HTC	Hydrothermal carbonization						
HTG	Hydrothermal gasification						
		Symbols					
		T	Temperature				
		t	Time				
		V	Volume				

Van der Waals forces. This kind of biomass typically has 30–60 weight percent cellulose, 20–40 weight percent hemicellulose and 15–25 weight percent lignin [11]. Different amounts of cellulose and hemicellulose in the structure of lignocellulosic biomasses such as canola stalk (CS), rice straw, and barley straw lead to their different behaviors in various conditions [12,13].

Biomass can be converted to value-added chemicals and fuels through new biomass conversion technologies such as thermo-chemical and biochemical processes [14]. In recent years, among various ways of thermo-chemical conversion, hydrothermal gasification was performed under subcritical (hydrothermal liquefaction) and supercritical water (hydrothermal gasification (HTG)) conditions provide the most advantageous method for producing high yields of H₂ and CO (synthesis gas) from high-moisture biomass [15]. Supercritical water (SCW) (P = 22.1 MPa, T = 374 °C) with its diversified physical and chemical properties, simultaneously acts as a non-polar solvent and reactant that can facilitate feed cracking [16]. On the critical point (P = 22.1 MPa, T = 374 °C) the dielectric constant of water reduces excessively; that leads to the non-polar behavior of water and overcomes its mass transfer limitations by providing a homogenous reaction media [17]. Furthermore, in HTG process, high energy consuming pretreatment of biomass such as drying is not necessary; besides produced gases via the HTG process have high-pressure which eliminates the repressurizing step for transportation [18]. HTG involves several reactions, a few of such reactions include steam reforming, water gas shift, and methanation reactions [19]. The main product of the steam reforming and water-gas shift (WGS) reactions is chiefly H₂ while CH₄ is the main product of the methanation reaction [20]. During HTG, SCW as the main factor in promoting the water-gas shift and steam reforming reactions significantly improves H₂ yield and hampers the formation of tar and char [8]. Recently there were many reports highlighting the impact of the control factors on the HTG of biomass [21], but surprisingly the impacts of biomass structure and the catalyst support on the process performance have not been studied widely.

In previous studies, it was approved that non-catalyzed HTG can be effective only when the reaction temperature is high [22]. On the contrary, catalyzed HTG yields higher H₂ and CO recovery even at lower reaction temperatures [23]. According to the literature, HTG has been performed with various catalysts such as Alkali (NaOH, KOH, K₂CO₃, Na₂CO₃, etc.) and supported transition metals as the main categories of homogeneous and heterogeneous catalysts, respectively [24,25]. In point of fact, recovering alkali catalysts from wastewater is a high-energy-consuming process and they exhibit lower H₂ and CO selectivity compared to supported transition metals [4]. Therefore,

adopting proper heterogeneous catalysts in biomass HTG process not only avoids the harsh conditions of SCW (high temperatures and pressures) but also significantly improves the gasification efficiency at lower temperatures and leads to an economically suitable conversion process [26].

It has been demonstrated that supported noble metals such as Ni, Pt, Pd, and Ru have a good catalytic activity in biomass, tar and char gasification to hydrogen and syngas [27]. They accelerate water-gas shift reaction to produce H₂ and show high physical and chemical stability in a supercritical water environment [28]. Although all the mentioned supported noble metals perform perfectly in the HTG of biomass, supported Ni catalysts are more frequently examined among the others due to their higher catalytic activities, better stabilities and especially their low-cost [29]. Some other metals (i.e. Ru, Co, and Cu) in low content can promote nickel catalytic performance in this process [30]. For example, It has been reported that cobalt has special properties to accelerate water-gas shift reaction and decelerate methanation reaction [31]. Moreover, Sato et al. investigated the effects of different carbon supported noble metals in subcritical and supercritical water media [32]. Their research proved that Ru/C have higher activity compared to Pt/γ-Al₂O₃. Therefore, selecting a suitable support among different porous materials such as Activated carbon (AC), γ-Al₂O₃, silica and graphene nano sheets (GNS) for designing the most hydrothermally stable catalyst in the HTG process has attracted enormous interest [33]. Recently, GNS with a carbon two-dimensional structure has attracted many attentions due to their extraordinary electrical, thermal and mechanical properties as well as their high specific surface area that is necessary for technologies such as high frequency analog electronics [34] and single molecule sensors [35,36], nanocomposites [37], batteries [38], super capacitors [39], liquids crystal display [40], and hydrogen evolution reaction [41]. High surface area of GNS and their unique structure and physicochemical properties have introduced them as a very promising catalyst support [42]. In comparison, many studies have proved the comparable performance of noble metals (Ni, Pt, and Rh) supported on AC and GNS in the HTG process [42–44]. Ding et al. have demonstrated the higher catalytic activity of Ni/activated carbon (AC) catalyst (hydrogen yield increasing by 81%) among other catalyst supports such as MgO (62%), CeO₂/Al₂O₃ (60%) and Al₂O₃ (52%) [45]. Although AC can be a suitable alternative to GNS and γ-Al₂O₃ in the catalytic hydrothermal gasification (CHTG) of biomass, its structure and morphology need further improvements for achieving higher catalytic activity and maintaining hydrothermal stability [46]. Consequently, many of the recent researches have been dedicated to the synthesis of single metal dual support catalysts, and dual metal dual

support catalysts and their comparison with other catalysts such as gamma alumina in order to increase the process efficiency [47]. Yet the recent efforts are necessary but not sufficient and optimizing the control factors governing the HTG process beside the detailed investigation of the performance of the catalysts are highly required.

In this study, conversion of CS was performed in a stainless-steel batch reactor under SCW conditions to determine the impacts of the control factors governing the HTG process such as (temperature, time and feedstock concentration) and optimize them for the highest possible H₂ gas production. Different binary metal catalysts supported on GNS are prepared using Ni and different noble metals (Ru, Co, and Cu) as promoters via the impregnation method and their performances are compared in the HTG process, proving Cu as the most optimized catalyst promoter. Furthermore, to maximize the benefits of the CS as a widely grown agricultural waste, we used it as both the HTG feedstock and the basic material for the preparation of the catalytic materials operating in the same process. Therefore, CS underwent hydrothermal carbonization (HTC) treatment and post chemical activation for the novel production of the support material for Binary Ni-Cu catalyst in the HTG process. Furthermore, we deeply investigated the impact of the aforementioned catalysts on the product distribution and H₂ gas production (especially the effect of catalyst supports was studied). Multiple analytical techniques such as Inductively Coupled Plasma Atomic Emission Spectroscopy (ICP-AES), Temperature-programmed reduction (TPR), Brunauer–Emmett–Teller (BET), Transmission Electron Microscopy (TEM), Fourier Transform Infrared Spectroscopy (FT-IR), and X-ray powder diffraction (XRD), Field Emission Scanning Electron Microscopy (FESEM) were conducted to study the physicochemical properties of the catalysts.

2. Experimental

2.1. Feedstock characterization and materials

CS was sampled in April 2017 from a farm located in the suburbs of Sari, Mazandaran, Iran. It was air dried before transportation to the laboratory. In the laboratory it was washed, dried at 120 °C for 24 h and was grounded and sieved in order to reach a powder of approximately 150 microns in diameter. The elemental analyses of CS were performed using a CHNS analyzer (Vario ELIII by Elementary, Germany) to determine its elemental structure and the corresponding results are presented in Table 1. This table also contains cellulose, hemicellulose and lignin contents of the CS which had been measured by TAPPI regulations. The weight percentage of oxygen was also calculated by the Eq. (1):

$$O\% = 100 - C\% - H\% - N\% - S\% - Ash\% \quad (1)$$

Moreover, the TGA analysis was also evaluated to further shed light on the amounts of ash, volatile matter and fixed carbon of the CS through introducing it into a thermogravimetric analyzer (TGA/SDTA851 and METTLER-TOLEDO compact) under the nitrogen atmosphere at the temperatures in the range of 30–800 °C with a heating rate of 10 °C·min⁻¹.

Nickel nitrate hexahydrate salt, Ni(NO₃)₂·6H₂O, with 99% purity, Ruthenium nitrosyl nitrate solution, Ru(NO)(NO₃)₃, with 1.5 wt% ruthenium and a density of 1.07 g·ml⁻¹, copper acetate monohydrate salt, Cu(C₂H₃O₂)₂·H₂O, with 98% purity, Cobalt acetate extra hydrate salt,

Co(CH₃COO)₂, were all purchased from Sigma-Aldrich Company and used for the preparation of catalysts.

2.2. Preparation of the catalyst supports

2.2.1. Preparation of AC

In order to prepare a sustainable and cost-effective catalyst support, in this work, CS which was used as the HTG feedstock as well as the feedstock for the preparation of AC through hydrothermal carbonization (HTC) process. According to our recently published article, the optimal HTC condition in order to produce a hydrochar which is highly appropriate for catalyst support preparation was defined using the 3D surface diagram of desirability vs. T and t which accordingly suggested the point T = 260 °C, t = 120 min, with around 17.14 wt% of mass yield as the optimum operating condition [48]. Therefore, the carbonization experiment was carried out using the carbonization temperature of 260 °C and reaction time of 120 min as the main controlled factors. A hydrothermal 50 ml non-stirred stainless-steel horseshoe-shaped pipe reactor with approximate pipe diameter and length of 8 mm and 100 cm, was used in the HTC process. It is worth mentioning that the scheme of the HTC reaction unit is shown in Figure S.1. The reactor is heated by immersion in a neutral molten salt bath which its temperature was measured and controlled by a digital temperature indicator controller. Firstly, 3 g of CS powder and 15 ml deionized water were completely mixed before they were loaded into the reactor. Secondly, argon gas was pumped into the reactor immediately to evacuate any possible traces of existing oxygen. Thirdly, in order to prevent the possible leakage of materials due to high pressure, reactor outlets were sealed carefully. Finally, the reactor was fully immersed in the molten salt bath with the temperature of 260 °C for 120 min. At the end of the hydrothermal carbonization process, the reactor was cooled by being submerged in a cold-water bath that was located beside the molten salt bath. The products (mixture of solid and liquid phases) were discharged by a vacuum pump and were separated by centrifugation. The remaining solid materials (called Hydrochar) were washed with distilled water and dried for 12 h at 120 °C.

The obtained hydrochars were chemically activated using potassium hydroxide (KOH). With reference to the conventional KOH impregnation method, KOH and hydrochars were thoroughly mixed at a weight ratio of 2:1 [48]. The mixture was dissolved in deionized water and refluxed overnight at 70 °C. Furthermore, the solid phase was extracted by centrifugation and was stored in an oven at 60 °C for 8 h to be dried. A horizontal quartz tube reactor was used for the chemical activation of the obtained hydrochars at 700 °C under argon gas flow for two hours. The activated hydrochar was collected from the reactor after it was fully cooled to the lab's temperature, then washed with 10 wt% HCl until its pH became neutral. In the end, the activated carbon was dried in an oven for eight hours at 60 °C and the obtained black powder was used as the catalyst support in further experiments. It is worth mentioning that the mass yield of the following process was around 50 wt%.

2.2.2. Preparation of GNS

GNS were synthesized via Chemical Vapor Deposition (CVD) technique at research institute of petroleum industry and used as a catalyst support. This method used a quartz tube with a diameter of 50 mm and 120 mm length as an electric furnace. The furnace heating rate was

Table 1
Elemental, Structural, and Proximate analysis of CS.

Feedstock	Elemental Analysis %					Structural Analysis %			Proximate Analysis			
	C	H	O	N	S	Cellulose	Hemicellulose	Lignin	Ash	Moisture	Fixed Carbon	Volatile Matter
CS	52.59	5.67	40.5	0.42	0.31	38	29.42	20	2.95	5.03	29.80	61.54

* The variance of CHNS amounts from 100% is due to Feedstocks' Ash content.

programmable and its temperature raised up to 900 °C for 5–30 min. In order to promote the preparation process, methane and hydrogen gas with the ratio of 4:1 were used as carbon source and carrier gas, respectively. Furthermore, GNS were purified and oxidized by 30% HNO₃ at 120 °C for 14 h to increase the carboxylic and hydroxyl functional groups [49]. Finally, the synthesized GNS were washed, dried, and stored for further experiments.

2.3. Preparation of catalysts

The concentration of nickel, copper, cobalt, and ruthenium were adjusted for each catalyst as described in Table 2. The GNS and canola stalk derived-AC supported Ni catalysts were prepared through co-impregnation method respectively with Nitric acid (HNO₃) and the HNO₃/Catalyst supports molar ratio was fixed at 1 in all catalyst preparation procedures [50]. Accordingly, Ni (NO₃)₂·6H₂O, Ru(NO)(NO₃)₃, Cu (C₂H₃O₂)₂·H₂O, and Co(CH₃COO)₂ were weighed appropriately to match the designated catalyst compositions described in Table 2. Furthermore, the mixture was poured into two beakers separately, each containing 10 ml of deionized water and then the mixture was dissolved in deionized water by being stirred for 30 min at room temperature. Meanwhile, the designated amount of GNS was loaded into one beaker, while the other one was also loaded with the appropriate amount of AC accordingly. Afterward, the stirring procedure continued for 2 h at 80 °C until the water was evaporated. After the co-impregnation step, the remaining solid products were dried at 120 °C for 2 h and calcined at 400 °C under argon flow for 3 h and then were slightly exposed to the atmosphere during the cooling procedure.

2.3.1. Catalyst characterization

The amount of impregnated metal on the catalyst supports was measured by Varian VISTA-MPX inductively coupled plasma-optical emission spectrometry (ICP-OES) instrument. 0.02 g of the sample was dispersed in 5 ml of nitric acid (Merck 65%) and 5 ml hydrochloric acid (Chem-Lab, 37%). The temperature of the mixture was kept at 40–60 °C for 3 h. The resulting mixture was filtered and washed several times with distilled water. The filtrate solution was diluted with deionized water up to 250 ml. The specific surface area, average pore volume, and average pore radius of the supports and catalysts were measured by BET surface area analysis via an ASAP-2010 V2 Micrometrics -TriStarll system. Accordingly, the samples were degassed at 200 °C for 4 h under 50 mTorr vacuum and their structural parameters were calculated from the N₂ adsorption and desorption isotherms at 77 K. In order to confirm the successful formation of the desired functional groups on the surface of the catalyst supports, The FT-IR absorption technique was also conducted on a Bruker ISS-88 instrument. A smooth transparent pellet was made for both GNS and AC separately with 0.55% of each mixed with 95–99.5% of potassium bromide (KBr), and the infrared beam were passed through these pellets. XRD patterns of the calcined Ni20/GNS, Ni-Ru/GNS, Ni-Co/GNS, Ni-Cu/GNS, and Ni-Cu/AC catalysts were conducted with a Philips PW1840 X-ray diffractometer with monochromatized Cu/K radiation. The FESEM imaging was utilized to determine the surface characteristics and morphologies of the prepared catalyst supports via SIGMA VP-500 (ZEISS, Germany). The morphology of the supports and calcined Ni20/GNS, and Ni-Cu/AC catalysts were evaluated by TEM. Sample specimens for TEM experiments were prepared by ultrasonic dispersion of the catalysts in ethanol, and the suspensions were dropped onto a carbon-coated copper grid. TEM images were taken by a Philips CM20 (100 kV) transmission electron microscope equipped with a NARON energy-dispersive spectrometer with a germanium detector. Moreover, TEM images were used for the particle size determination of Ni particles impregnated on the calcined catalyst supports.

2.4. HTG setup and experimental outline

The HTG procedure is performed on the same setup of the HTC and the only difference between the two processes are the control factors. For non-catalytic tests, the designated amount of sample was added to the determined amount of deionized water to make a mixture. Before sealing the reactor, argon gas was pumped into the reactor immediately to evacuate any possible traces of existing oxygen. Furthermore, in order to prevent the possible leakage of materials due to the exponential increase of the reactor's pressure during the process by varying temperature from 0 to 440 °C (Fig. 1), reactor outlets were sealed carefully. After that, the reactor was fully immersed in the molten salt bath with the designated temperature controlled by a temperature indicator controller. At the end of the HTG process, the reactor was cooled by being submerged in a cold-water bath that was located beside the molten salt bath. In the case of catalytic tests, the reactor was loaded with the designated amount of catalyst. The catalyst was then reduced in hydrogen flow (50 ml STP/min H₂) for 3 h at the temperature that was in accordance with TPR analysis and then the feedstock and deionized water were added to the reactor, before immersing the reactor into the molten salt bath. After each experiment, the water-insoluble portion of the products was retrieved by filtration and collected for further analysis. The aqueous products were then transferred to a 10 ml centrifuge tube. After centrifugation, the top liquid phase was collected and stored at 4 °C prior to analysis.

2.5. Product analysis method

2.5.1. Analysis of the gaseous product

The amount of each gaseous product was measured and analyzed using gas chromatography (GC) (Varian 3400 and Teygostar-Compact) Equipped with a packed Proapak Q-S 80/100 column (length: 30 m, internal diameter: 0.53 mm and material: stainless steel), a methanizer and a Flame ionization detector. The detailed apparatus of the GC instrument and the analysis procedure can be found elsewhere in the previous investigations of our colleagues [51].

2.5.2. Analysis of the aqueous and solid products

The total organic carbon (TOC) levels and the mass yields of the liquid and solid products were also analyzed respectively, to investigate the impact of the control factors and catalyst types on the non-gaseous products. The aqueous phase of the HTG products was analyzed by a TOC analyzer (Shimadzu, TOC-L). The mass yield of solid residues was also measured by filtering the non-gaseous products obtained after the evacuation of the reactor.

Carbon gasification efficiency (CGE), Eq. (2), carbon liquefaction efficiency (CLE), Eq. (3), and carbon solidification efficiency (CSE), Eq. (4), as the proofs for a successful conversion of biomass were calculated by the equations described below [52]:

Table 2
Chemical compositions and preparation details of the calcined catalysts.

Sample	Ni targeted (wt%)	Promoter targeted (wt%)	Ni measured (wt%)	Promoter measured (wt%)	Average Crystallite size (nm) ^a
Ni10/GNS	10	0	9.8	0	–
Ni15/GNS	15	0	14.7	0	–
Ni20/GNS	20	0	19.9	0	17.7
Ni25/GNS	25	0	25	0	–
Ni-Ru/GNS	20	2 (Ru)	19.8	1.98	18.1
Ni-Co/GNS	20	2 (Co)	19.7	2.01	18.2
Ni-Cu/GNS	20	2 (Cu)	19.7	1.96	16.3
Ni-Cu/AC	20	2 (Cu)	19.9	1.98	11.1

^a Measured by XRD results.

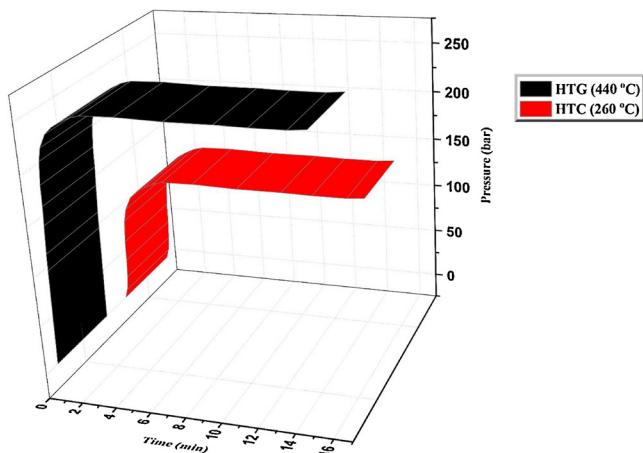


Fig. 1. Variation of HTG reactor's pressure versus time (F.C = 0.8 wt%) (Black), and Variation of the HTC reactor's pressure versus time (F.C = 0.8 wt%) (Red) (For interpretation of the references to colour in this figure legend, the reader is referred to the web version of this article).

$$CGE = \frac{(\text{carbon in gaseous products})}{(\text{carbon in CS})} \quad (2)$$

$$CLE = \frac{(\text{carbon in Liquid products})}{(\text{carbon in CS})} \quad (3)$$

$$CSE = \frac{(\text{carbon in Solid products})}{(\text{carbon in CS})} \quad (4)$$

Eventually, carbon conversion efficiency (CCE) can be calculated via Eq. (5) as follows:

$$CCE = CGE + CLE + CSE \quad (5)$$

3. Results and discussion

3.1. Feedstock characterization

The elemental, structural, and proximate analysis of the CS is performed and the results are shown in Table 1.

In brief, CS has a high amount of carbon and cellulose, the two parameters that made CS a suitable feedstock for the HTC and chemical activation process. Moreover, according to the results obtained by the

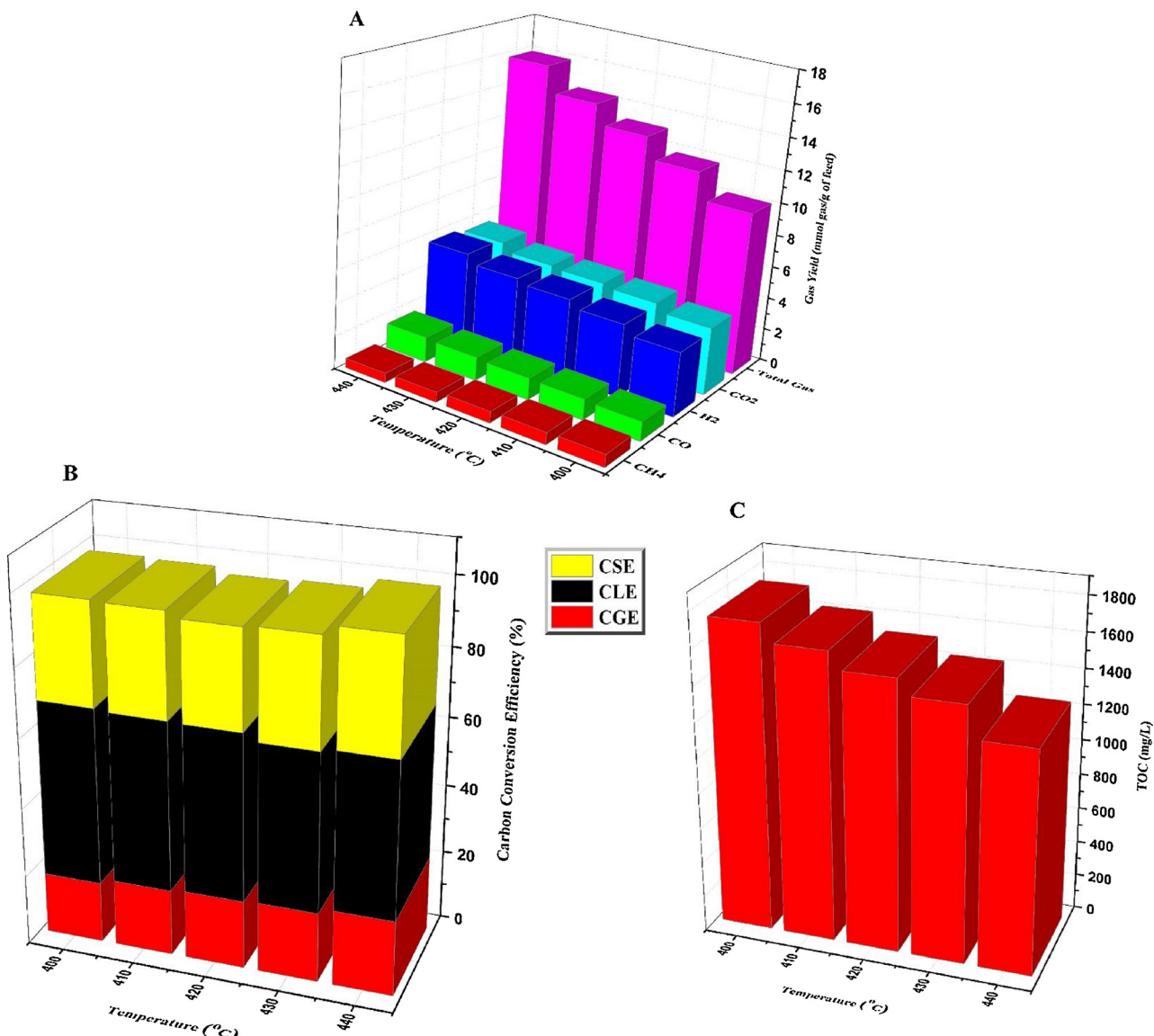


Fig. 2. Variation of; A) Individual and total gas yield, B) CSE, CLE, and CGE, and C) TOC of the aqueous phase with Temperature (t = 20 min, F.C = 2.4 wt%).

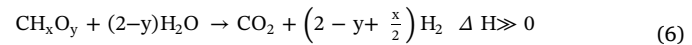
proximate analysis, the low amount of ash content and high amount of fixed carbon make CS as a high potential waste to use as support materials after some pretreatments (including HTC and activation procedures). The TGA/DTG diagram of CS is also shown in **Figure S.2**, demonstrating a peak that occurs below 200 °C which suggests a weight loss that is mainly due to the drying and release of moisture. Another primary weight loss determined by a sharp peak located at 300 °C is also attributed to the decomposition and devolatilization of hemicellulose in the CS sample. The final peaks observed in the figure might also be attributed to the decomposition of other solid residues [53].

3.2. Optimizing the control factors in non-catalytic HTG

3.2.1. Temperature optimization

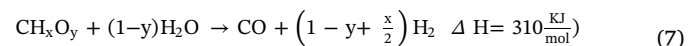
In order to investigate the impact of the operational parameters (temperature effect, reaction time effect, and feedstock concentration effect) on the production yield of the gaseous products, non-catalytic HTG of the CS was performed. In consequence, the effect of temperature in HTG of ICS was investigated with the temperature variation of

400–440 °C while the reaction time and feed concentration were fixed at 20 min and 2.4 wt%, respectively. On the other hand, the reaction procedure of biomass gasification in SCW media has found to be complicated and cannot be explained very well [54], but the overall chemical conversion can be summarized by the reaction shown below:

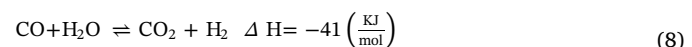


Further to this, the occurrence of some competitive reactions indicate the generation of the main final products as they are given below:

Steam Reforming:



WGS:



Methanation:

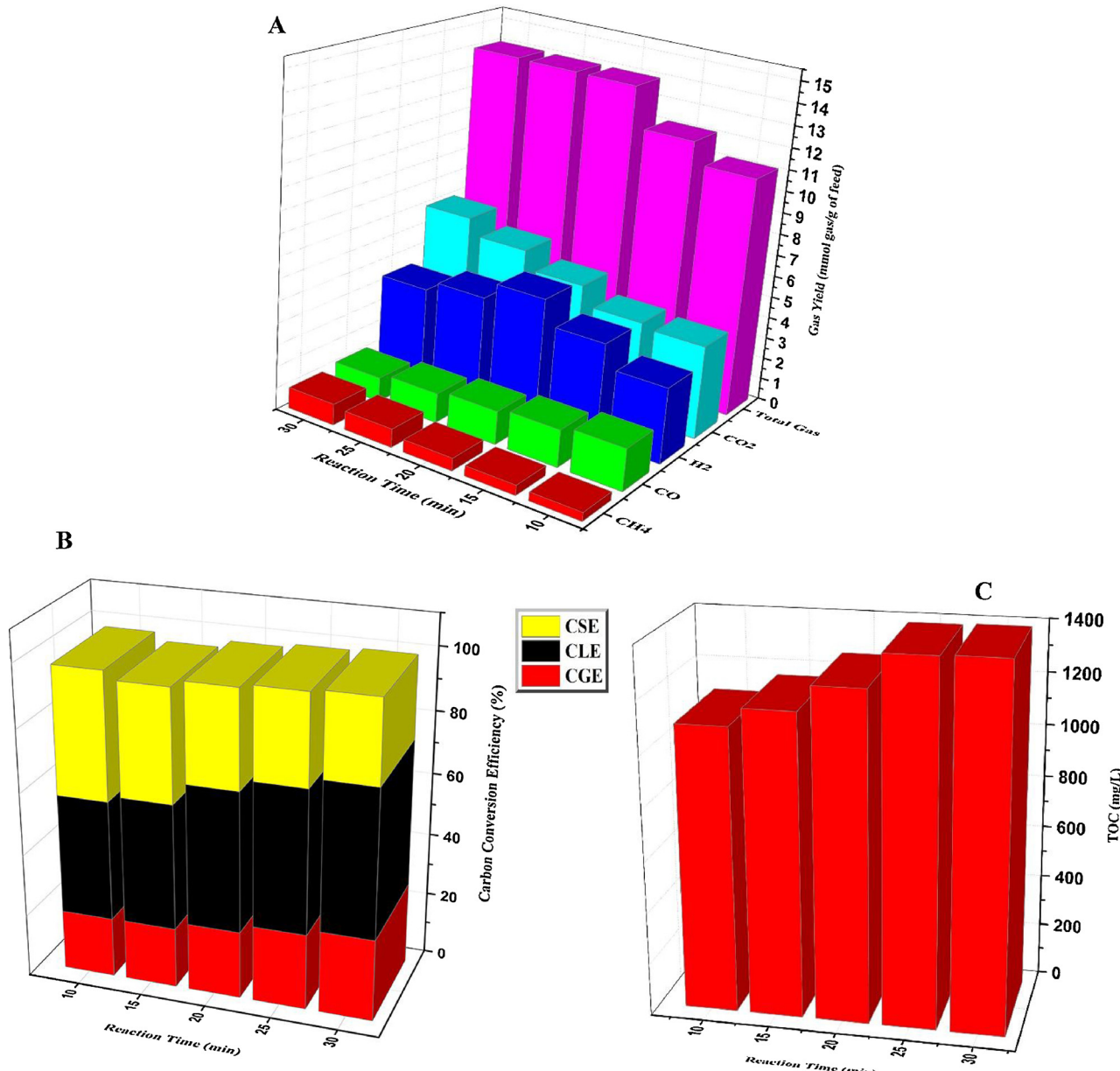
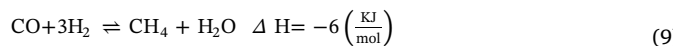


Fig. 3. Variation of; A) Individual and total gas yield, B) CSE, CLE, and CGE, and C) TOC of the aqueous phase with Reaction Time (T = 440 °C, F.C = 2.4 wt%).



Furthermore, Fig. 2A demonstrates the effect of reaction temperature on the major gaseous products (H_2 , CO_2 , CO , and CH_4) and the total gas yields. Accordingly, increasing temperature from 400 to 440 °C has increased the total gas yield by a factor of 1.57 which could be attributed to an enhancement of the endothermic reforming reaction of CS in SCW media (Eq. (7)) [55].

Moreover, the obvious increase in the temperature leads to an increase in H_2 , CO_2 and CO yields by the factors of 1.44, 1.3 and 1.31 respectively which may be the result of a successful promotion in the highly endothermic steam reforming and overall reactions (Eqs. (6), and (7)). In contrast, the Methanation (Eq. (9)) is an exothermic reaction, increasing the temperature may lead to its deceleration that results in the smooth decrease of CH_4 yields (by the factor of 0.74) as it is demonstrated in Fig. 2A [56]. Furthermore, due to the endothermic nature of the overall reaction, it can be concluded that the best temperature for achieving the highest H_2 and CO yields, is the highest possible temperature which was 440 °C in this project.

In addition, the weight percentage variation of the converted carbon, gaseous, aqueous and solid phase products with the variation in temperature are demonstrated in Fig. 2B. According to this figure, as temperature increased from 400 to 440 °C, the amount of CGE increased while the other parameters (CLE and CSE) decreased smoothly. This behavior was expectable and can be attributed to better gasification of

biomass in higher temperatures through intensive endothermic steam reforming reaction (Eq. (7)) which results in the remaining of less solid residue and aqueous products [57].

Assuming that some amounts of hydrocarbon may have still stuck on the inner wall of the batch reactor, it was not possible to collect the products ultimately which explains the observed error in carbon balance.

Moreover, TOC analysis data were also represented in Fig. 2C, which significantly confirm the mentioned phenomena. In addition, the TOC level decreased by increasing reaction temperature, suggesting the decrease of organic chemicals in liquid phase achieved at higher reaction temperatures [58].

3.2.2. Reaction time optimization

In order to study the effects of the reaction time on the HTG process, the time parameter was varied from 10 to 30 min while other control factors were kept constant. Hence, Fig. 3A demonstrates the total gas yield besides the yields of each individual gas product versus time. The results suggested that the amount of total generated gas increased by increasing the reaction time from 10 to 20 min by a factor of 1.25, but no significant change in the amount of total gas was observed by extending the reaction time to 30 min. Further to this, the hydrogen gas yield increased by increasing the reaction time up to 20 min and then started to decrease. Therefore, 20 min was chosen to be the optimum time for hydrogen production in the time interval of 10 to 30 min.

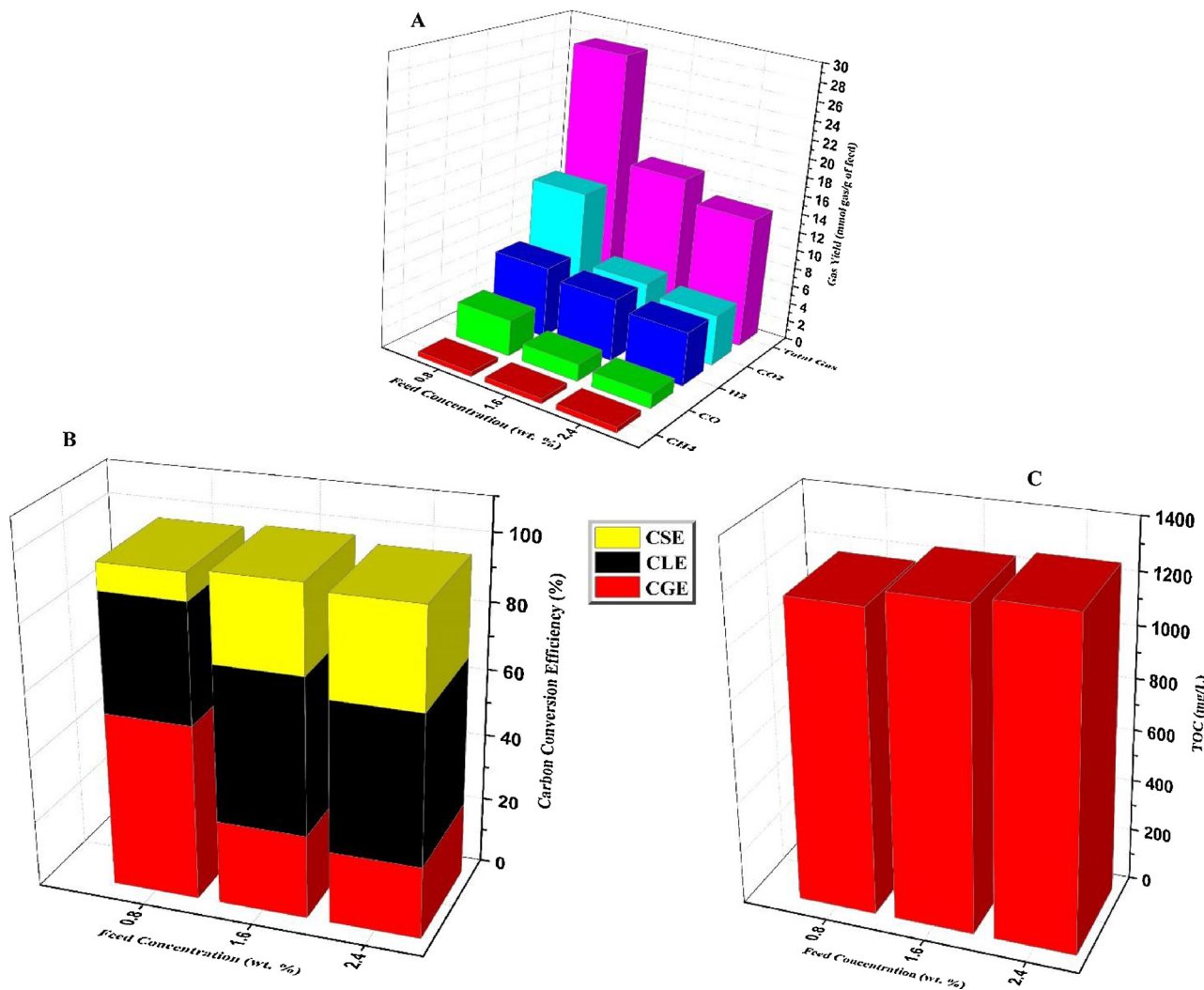


Fig. 4. Variation of; A) Individual and total gas yield, B) CSE, CLE, and CGE, and C) TOC of the aqueous phase with Feed Concentration ($T = 440$ °C, $t = 20$ min).

Also, it can be inferred from this figure that increasing reaction time up to 20 min has a positive impact on H₂ gas yield (from 3.48 to 5.65 mmolgas. g_{CS}⁻¹), it is also observed that extending the reaction time from 20 to 30 min increases the methane yield from 0.57 to 0.96 mmolgas.g_{CS}⁻¹. On the contrary, the H₂ gas yield decreased due to the probable superiority of the methanation reaction (Eq. (9)) in the mentioned time interval [59]. The observed stability in the total gas yield when reaction time takes more than 20 min is the further proof of the mentioned phenomenon. Since the objective of biomass gasification in SCW is H₂ production, methanation reaction must be restrained and WGS reaction (Eq. (8)) must be enhanced. According to Eq. (6), generating one mole methane consumes 3 mol of H₂ and 1 mol of CO, thus downward trend of H₂ yield should be sharper than rising trend of CH₄ and the downward trend of CO yield.

The distribution of the HTG products in solid, liquid and gas phases versus reaction time is also represented in Fig. 3B. According to this figure, as reaction time increased from 10 to 30 min, CGE increased smoothly by a factor of 1.36, which is in total agreement with the enhancement of total gas yield in Fig. 3A. More interestingly, increasing reaction time provides more opportunity for the gaseous and high molecular weight products to polymerize, thus promoting the generation of aqueous products [60]. The increment in CLE amount in Fig. 3B as the reaction time increased from 10 to 30, perfectly confirms the aforementioned phenomena.

Moreover, TOC analysis data were also represented in Fig. 3C, depicting the increase in the TOC level by increasing reaction time. The authors believe that this observed phenomenon was due to the more decomposition of CS and its lignocellulosic structures at higher reaction times, resulting in higher transition of carbon fragments into the liquid

phase.

3.2.3. Feedstock concentration optimization

We also investigated the impact of CS initial concentration on the HTG process and the results are shown in Fig. 4. In this section, three different concentrations of CS were used (0.8, 1.6 and 2.4 wt%) while other control factors were kept constant. According to Fig. 4A, increasing the CS concentration from 0.8 to 2.4 wt% had a negative impact on the total gas yield (mmolgas.g_{CS}⁻¹) by decreasing it from 27.76 to 13.9 (mmolgas. g_{CS}⁻¹). Also, hydrogen, CO₂, and CO gas yields decreased by a factor of 0.75, 0.38 and 0.4, respectively.

Furthermore, by increasing the CS concentration, it is obvious that the ratio of water/biomass content in the reactor will decrease which prevents the steam reforming reaction, consequently decreases the CS conversion and gas yield. Yet, at low water to carbon ratios, due to consumption of CO and H₂, methane gas yield slightly increased. These results are in reliable agreement with the results reported by other researchers [61–64]. It has been reported that gasification of biomass feedstocks with higher biomass concentrations are much more difficult than those with lower biomass contents [65]. Moreover, the results of CCE and TOC versus feed concentration variation are presented in Fig. 4B and C, respectively.

As seen in the Fig. 4B, as CS concentration increases from 0.8 to 2.4, CGE decreases and CLE increases simultaneously. In conclusion, the hydrolysis of a feedstock with a higher biomass to water ratio has been proven to be more difficult and as a result, a great part of feedstock remains unconverted as a solid residue, suggesting the operational suitability of a feedstock with minimum concentration. The opposite view is when considering the industrialization of HTG process as a

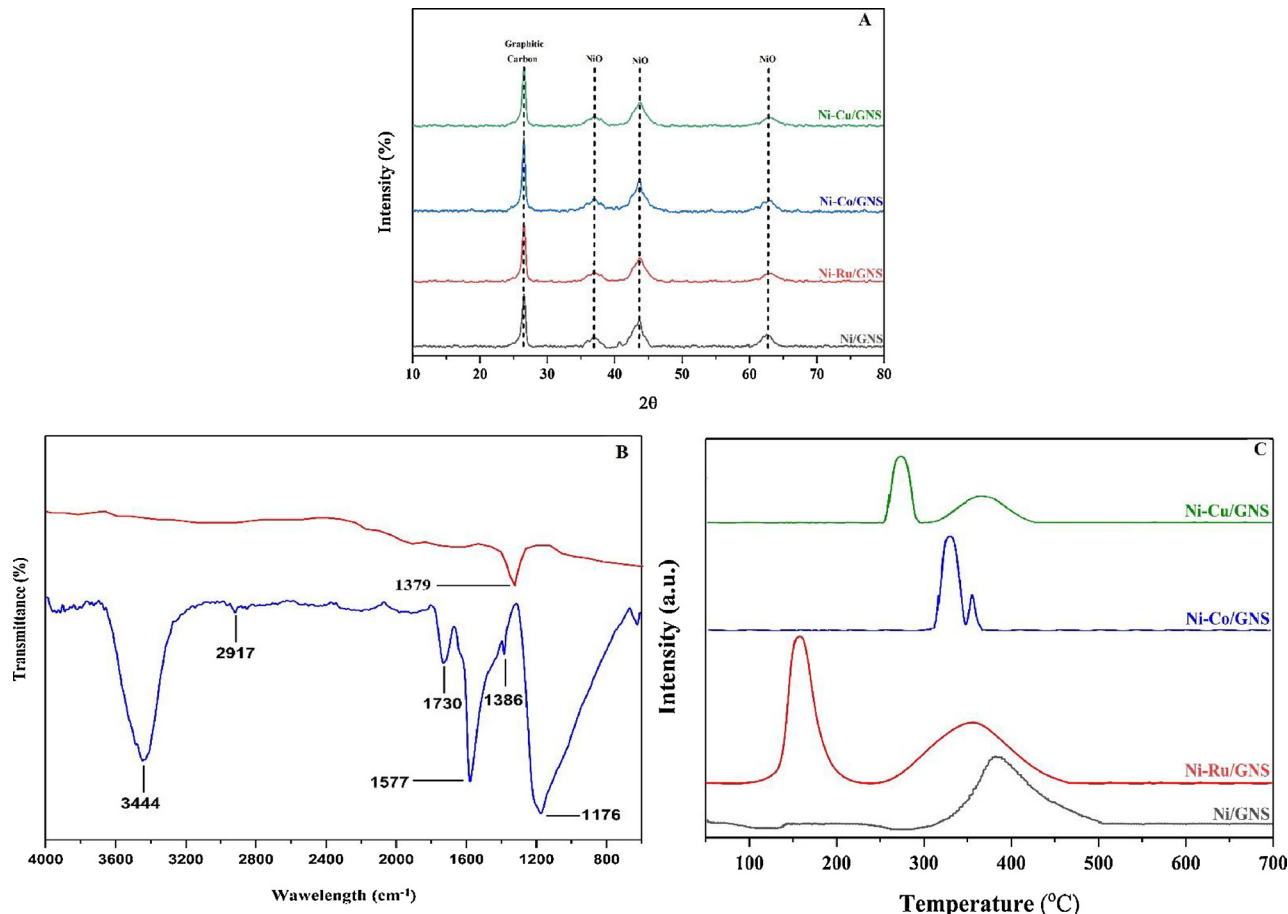


Fig. 5. Surface Morphology and chemistry analyses results of GNS supported catalysts (Ni20/GNS, Ni-Ru/GNS, Ni-Co/GNS, and Ni-Cu/GNS); A) XRD, B) FT-IR, and C) H₂-TPR.

priority and due to its high energy consuming procedure, selection of the minimum feedstock concentration as the optimum amount for the HTG process is obviously not cost-effective. Hence, here we selected a feed concentration of 1.6 wt% as the optimal concentration.

3.3. Comparing the morphology and the activity of the HTG catalysts

In order to enhance the efficiency of the HTG process, the gasification of CS was performed using several catalysts with various promoters and especially two different supports. As a blank test, pure GNS and pure AC were tested separately to indicate the impact of HTG on the catalyst supports. According to the results, no significant gasification of GNS and AC were observed in the mentioned operating condition. In consequence, the catalyst supports exhibited high stability in the hydrothermal gasification process [66,67] thus they were applied to promote the conversion of CS in the same aforementioned conditions of the optimum non-catalytic experiments.

3.3.1. Structure and morphology of the bimetallic Ni-M/GNS ($M = Ru, Co, Cu$) catalysts

The actual metal content of the catalysts was measured by ICP measurements and the results (reported in Table 2) indicate very close values to the desired ones, suggesting the successfulness of the co-impregnation procedure.

The corresponding N_2 adsorption isotherms at 77 K of all the samples (Ni10/GNS, Ni15/GNS, Ni20/GNS, Ni25/GNS, Ni-Ru/GNS, Ni-Co/GNS, Ni-Cu/GNS, Ni-Cu/AC) are shown in Figure S.3, suggesting a combination of Type I and Type IV isotherms, with apparent narrow H1-type hysteresis loops which according to the IUPAC classification define the characteristic of both micro- and mesoporous materials with relatively narrow pore size distributions (PSD) or some spherical particles with uniform geometry sizes [68]. Further analysis also proved the existence of reasonably narrow PSDs in the range of 4.4–5.4 nm.

Fig. 5A presented the XRD patterns of Ni20/GNS, Ni-Ru/GNS, Ni-Co/GNS, and Ni-Cu/GNS catalyst samples. The peaks located at $2\theta = 26^\circ$ correspond to graphite diffractions [69]. All the samples demonstrated three strong diffraction peaks around $2\theta = 37.5^\circ, 43.3^\circ$, and 62.9° corresponding to the reflections of NiO crystalline planes [70,71]. Accordingly, broad diffraction peaks observed in the XRD patterns of the samples were associated to the cubic NiO phase in the amorphous form [72]. On the contrary, the corresponding XRD patterns of the GNS supported catalysts demonstrated stronger diffraction peaks that were related to the NiO phase with large crystalline particles as expected [73].

The average crystallite size of NiO was calculated using Debye-Scherer equation. The results of the average crystallite sizes shown in Table 2 proved that addition of a second metal as a promoter (especially Cu) would decrease the average crystallite size of NiO. These results are in agreement with the larger particles of Ni or NiO in the GNS supported structure (shown in TEM analysis, Fig. 6). Moreover, the broad diffraction peaks in the XRD patterns of the catalysts are also attributed to the existence of large exposed surface. Ru, Co, and Cu particles corresponding diffractions were not observed in the XRD spectra which could be explained by several reasons: (i) the particles may be too well dispersed on the catalyst supports to be detected [74], (ii) the particles may be amorphous. In addition, the surface areas of the catalysts are similar, $307 \text{ m}^2 \text{ g}^{-1}$ for Ni20/GNS and $261 \text{ m}^2 \text{ g}^{-1}$ for Ni-Ru/GNS, $263 \text{ m}^2 \text{ g}^{-1}$ for Ni-Co/GNS, $258 \text{ m}^2 \text{ g}^{-1}$ for Ni-Cu/GNS, and $195 \text{ m}^2 \text{ g}^{-1}$ for Ni-Cu/AC samples. Thereby, we can conclude that the loading of nickel through the co-impregnation method had an unremarkable impact on the total surface area of the catalysts [75].

The FT-IR spectra of the functionalized Graphene were recorded and the results are shown in Fig. 5B. With reference to the achieved FT-IR spectra, the presence of Peaks at 1050, 1370, 1720 and 3440 cm^{-1} which are attributed to the stretching of epoxy(C=O), ether (C-O), carbonyl (C=O) and hydroxyl (–OH) groups [16] (along with a sharp

peak at 1630 cm^{-1} which is attribute to alkenyl stretching in the main structure of GNS (C=C)), prove that nitric acid treatment was successful and the desired functional groups were added to GNS surface which was necessary for increasing the dispersion of metals [76]. Also, the mentioned functional groups can prevent the sintering of metal particles during the calcination reaction [77].

Fig. 5C presents the H_2 -TPR profiles for the as-deposited mono- and bimetallic promoted Ni-based catalyst samples before H_2 reduction. Ni-Ru, Ni-Co and Ni-Cu bimetallic catalysts supported on GNS displayed bimodal reduction peaks at around 160 and 350°C , which are attributed to the reduction of $\text{Ru}^{3+} \rightarrow \text{Ru}^{2+}$, $\text{Ru}^{2+} \rightarrow \text{Ru}^\circ$ [78], $\text{Co}^{2+} \rightarrow \text{Co}^\circ$ and $\text{Cu}^{2+} \rightarrow \text{Cu}^\circ$ [79], respectively. The peak corresponded to the Monometallic Ni/GNS presented a small reduction peak centered at around 380°C . While in the case of Ni-Ru/GNS, Ni-Co, and Ni-Cu, bimodal reduction peaks were exhibited at around 160, 330 and 360°C . There was no significant shift observed in the reduction profiles of the promoted catalyst which significantly proves that the Ru, Co, and Cu atoms do not couple with Ni on the surface of GNS, suggesting the presence of Ni particles in segregated form rather than the bimetallic structure [80].

Furthermore, the TEM image of the Ni20/GNS sample was given in Fig. 6. The average particle sizes were calculated and presented in Table 3 by using the TEM images and measuring the sizes of observed individual particles.

TEM image (Fig. 6) presented the heterogeneously distributed and aggregated Ni and/or NiO nanoparticles on the surface of GNS support. Accordingly, Nanoparticles as small as 10 nm could be observed in the image of the heterogeneously distributed Ni20/GNS catalyst along with some large particles of around 20 nm, with the estimated mean particle size being 18.5 nm.

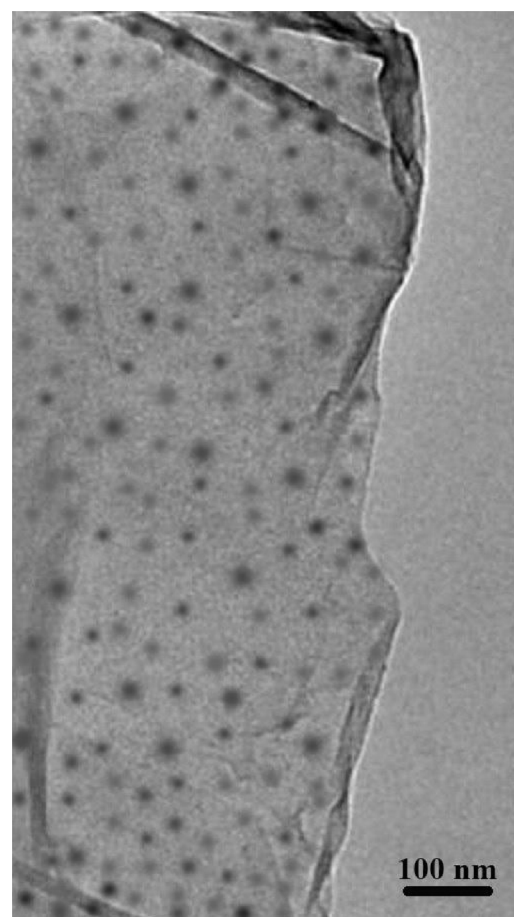


Fig. 6. TEM image of Fresh calcined Ni20/GNS catalyst.

Table 3
BET surface area and average pore size diameter results.

Sample	S_{BET} ($\text{m}^2 \cdot \text{g}^{-1}$)	Pore volume ^a ($\text{cm}^3 \cdot \text{g}^{-1}$)	Average pore Diameter(nm)	Average Particle Size ^b (nm)
GNS	602	0.66	4.4	—
AC	474	0.29	1.3	—
Ni10/GNS	422	0.51	4.7	—
Ni15/GNS	353	0.45	4.9	—
Ni20/GNS	307	0.43	5.1	18.5
Ni25/GNS	287	0.41	5.3	—
Ni-Ru/GNS	261	0.40	5.4	—
Ni-Co/GNS	263	0.40	5.4	—
Ni-Cu/GNS	258	0.40	5.4	—
Ni-Cu/AC	195	0.23	1.9	12.3

^a Single point.

^b Calculated by TEM results.

3.3.2. Activity of the Ni-M/GNS ($M = \text{Ru, Co, Cu}$) catalysts in optimized HTG condition

In order to study the impact of the co-impregnated catalysts on hydrogen yield, non-catalytic experiments were performed first and then compared to the catalytic experiments under the optimum operational conditions achieved in non-catalytic experiments. Therefore, HTG of 1.6 wt% CS was performed in the presence of catalysts with different Ni loadings (monometallic catalysts including Ni(10–25)/GNS) at 440 °C for 20 min. Fig. 7 demonstrates the total gas yield besides the yields of each individual gaseous product (mmolgas.g.cs^{-1}) obtained from the HTG process in the presence of GNS supported catalysts.

According to Fig. 7, the total gas yield significantly increased when the gasification of CS was performed in the presence of catalysts. By using Ni10/GNS, Ni15/GNS and Ni20/GNS catalysts, H_2 gas yield increased by the factors of 1.62, 1.74 and 2.02, respectively. However, by increasing the Ni loading to 25 wt% (Ni25/GNS catalyst) no significant change in the H_2 gas yield was observed. This phenomenon could be due to the blockage of support pores by using higher metal loading for the Ni25/GNS catalyst (it was confirmed by BET results) [81]. These results proved that GNS acts as an efficient and stable support for Ni catalyst in HTG of CS, with the optimum Ni loading of 20 wt%. Ni enhances H_2 , CO, and CO_2 production by promoting the reforming reaction. On the other hand, it can also enhance methane production and decrease CO and H_2 production by accelerating the methanation reaction [82]. Regardless of the fact that, H_2 is consumed in the methanation reaction, an increase in the H_2 generation is observed after increasing Ni loading from 10 to 20 wt%. In short, the impact of Ni on reforming reaction is more important and apparent compared to its effect on the methanation reaction [83].

3.4. Achieving the optimized GNS supported catalyst promoter

In order to optimize and compare the performance of the commonly utilized catalyst promoters (Ru, Co, and Cu) these metals were used for the promotion of Ni20/GNS catalyst performance. HTG of CS with the concentration of 1.6 wt% was performed in the presence of promoted catalysts at 440 °C for 20 min. Fig. 7 also demonstrates the total gas yield (mmolgas.g.cs^{-1}), and the yields of H_2 , CO, and CO_2 obtained from the CHTG of CS in the presence of promoted (Ni-Ru/GNS, Ni-Co/GNS, and Ni-Cu/GNS) catalysts. As shown in this figure and in comparison with Ni20/GNS catalyst, Ru promoted catalyst increased the total and H_2 gas yield by factors of 1.26 and 1.31, respectively. Role of Ru as an active metal in the breaking of the C–C bond is highly effective, thus it can perfectly promote the production of all the gaseous products through the cleavage of existing C–C bonds in the biomass structure with the help of SCW media [84]. Also, Ru has a serious impact on the promoting of methanation reaction.

The impacts of cobalt and copper as catalyst promoters are also shown in Fig. 7. It is apparent that they had a slightly positive effect on the total gas yield (mmolgas.g.cs^{-1}) and H_2 gas yield. However, the effect of copper was more obvious. These two promoters are capable of accelerating the WGS reaction and decelerating the methanation reaction [85]. For this reason, cobalt and copper were able to prevent the formation of methane, resulting in the higher production of gases with lower amounts of methane compared to the unprompted catalysts. According to the previous reports, copper helps to disperse Ni particles on the surface of the catalyst support and therefore, promotes the production of H_2 [86,87]. In agreement with the mentioned results, the data shown in Table 2 also demonstrated that using copper as the catalyst promoter resulted in the size reduction of the average metal particles from 17.7 to 16.3 nm and consequently increased the dispersion percentage. Among the three different promoters used in this project, copper proved its superiority by promoting the WGS reaction, decelerating methanation reaction, promoting the reforming of methane, and producing the highest yield of H_2 gas and the lowest amount of methane gas. By showing the best performance as a catalyst promoter, it was selected as the optimum promoter for the further investigations.

Furthermore, to estimate the impact of promoter additives on the catalytic activity of Ni active sites, the turnover frequency (TOF) was calculated (Figure S.5.) using the data obtained through H_2 -Chemisorption analysis (detailed description is available in supplementary data, Table S.1). According to the TOF results, it is clearly observed that the promotion of GNS supported catalysts with Ru, Co, and Cu metals lead to an increase in the activity of individual active catalytic sites in comparison with unprompted Ni catalyst (Ni20/GNS) in the reaction medium. Since the TOF data were calculated by CGE amounts (Equation S.2.), the H_2 selectivity was also reported (Equation. S.1.) to show the catalyst activity toward the main goal of the present work, that is the H_2 production. According to other results presented in Table S.1., it could be inferred that the addition of promoter to the catalyst has resulted in various outcomes such as the change in the number of catalytic sites, plus the dispersion and the interaction between active sites and GNS as the support. For example, the addition of the aforementioned promoters to Ni20/GNS catalyst lead to a higher number of active sites (in the range of 3–5 ($\times 10^{18}$) more active sites) and their dispersion on the support surface [88]. On the contrary, as it was mentioned above, the data obtained from the H_2 -TPR analysis

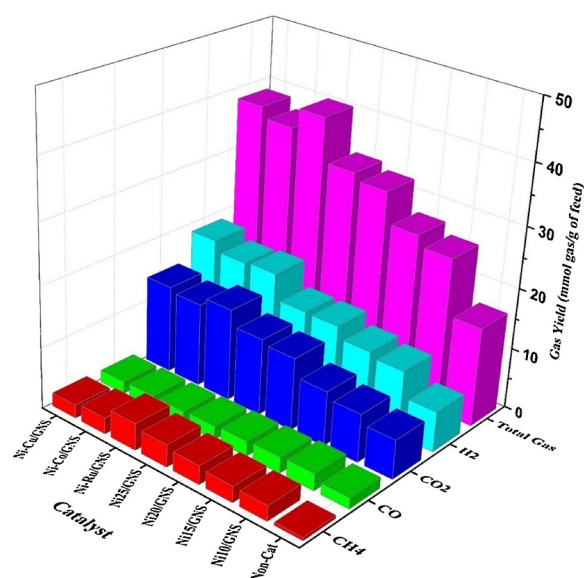


Fig. 7. Individual and total gas yields obtained from the HTG process in the presence of GNS supported catalysts.

(calculated from Fig. 5C) revealed the slight influence of the promoter addition to the GNS supported catalysts. In conclusion, it can be deduced that the promotion of GNS supported Ni catalysts with Ru, Co and Cu has a moderate impact on the TOF, H₂ selectivity and total gas yields. The better behavior of promoted catalysts toward HTG process could be originated from an increase in the number of the active sites and their dispersion due to the H₂-chemisorption results [89].

3.5. Investigating and comparing the activity of Ni-Cu/AC catalyst with Ni-Cu/GNS

In the previous section, we compared the activity of GNS supported catalysts according to the variation in their achieved gas yields and TOF at the temperature of 440 °C and 20 min and the results are shown in Fig. 7. With reference to the optimum operational conditions achieved from previous experiments, the AC was used as the catalyst support instead of GNS without changing other optimum conditions. Accordingly, the HTG of 1.6 wt% CS was performed at 440 °C for 20 min in the presence of 20 wt% Ni and copper as promoter supported on AC. The carbon efficiency and gas yields corresponding to Ni-Cu/AC catalyst were also measured and the results were depicted in Fig. 8. This figure only displays the gaseous yields of H₂, CH₄, CO, and CO₂, while other gaseous components such as C₂H₄, and C₂H₆ were not contained in this figure. The addition of the Ni-Cu/AC catalyst greatly enhanced the gasification reaction of CS under the optimum operating conditions as the results related to this sample represent a high enhancement of carbon gasification efficiency (more than 62%) which is comparable to the similar catalysts supported on GNS (Ni-Cu/GNS).

The H₂ gas yield achieved while utilizing Ni-Cu/AC catalyst is 19.96 mmolgas. g_{CS}⁻¹, indicating the high selectivity of this catalyst toward hydrogen gas production. The Ni-Cu/AC catalyst also gave a smooth decrease in CH₄ yield (from 2.19 mmolgas. g_{CS}⁻¹ in Ni-Cu/GNS to 1.59 mmolgas. g_{CS}⁻¹ in Ni-Cu/AC) while CO₂ (increased from 2.02 mmolgas. g_{CS}⁻¹ in Ni-Cu/GNS to 2.89 mmolgas. g_{CS}⁻¹ in Ni-Cu/AC) CO₂, (increased from 14.34 mmolgas. g_{CS}⁻¹ in Ni-Cu/GNS to 17.21 mmolgas. g_{CS}⁻¹ in Ni-Cu/AC) and H₂ (increased from 18.94 mmolgas. g_{CS}⁻¹ in Ni-Cu/GNS to 19.96 mmolgas. g_{CS}⁻¹ in Ni-Cu/AC) production was enhanced in the presence of this catalyst. The observed variation can be attributed to the impact of Ni-Cu/AC catalyst in the acceleration of the WGS reaction and constraining the methanation reaction simultaneously.

In order to shed more light on the catalytic activity of the active sites in the case of the applied catalysts in the current work, the Turnover Frequency (TOF) was calculated (Figure S.5.) as it was mentioned earlier. According to Figure S.5., it is clearly observed that the TOF results of the Ni-Cu/AC catalyst is slightly higher than others (GNS supported) while this difference in H₂ selectivity is more significant in comparison. Finally, the CCE of all the catalysts were also calculated based on Eq. (5) and the results are shown in Figure S.4. As the catalysts and the HTG feedstock were all carbon based, the amount of solid product was calculated via the subtraction of catalyst amount from the whole amount of solid residue evacuated from the reactor after HTG process. According to this figure, the higher Ni content in the catalyst has resulted in higher gasification efficiency due to the activity of this metal in gasification process. The activity of the Ni based catalysts has been promoted by the utilization of other highly active elements that were Ru, Co and Cu. By the way, the promotion of Ni catalysts with Ru, Co and Cu metallic elements has shifted the CCE to higher gaseous products as well as some reduction in CSE and CLE amounts. Among these promoters, Ru has the highest activity in this area which is originated from the activity of Ru in methanation reaction alongside with Ni activity in gasification step. In comparison with GNS supported catalyst, Ni-Cu/AC catalyst shows better activity in the case of CGE which could be explained by the TOF results. According to these results, Ni-Cu/AC has higher number of active catalytic sites per gram of catalyst alongside with higher amount of TOF which could

completely justify the difference in CGE content.

3.6. Structure and morphology of the bimetallic Ni-Cu/AC catalyst

In order to investigate the superiority of AC supported catalyst (Ni-Cu/AC) over its counterpart catalyst supported on GNS (Ni-Cu/GNS), some structural and morphological analyses were done. Fig. 9A displays the XRD results of the crystalline Ni (20%)/AC, and Ni (20%) – Cu (2%)/AC catalyst for better determination and comparison of their structure. Accordingly, the diffractions peaks (at 27 and 33°) are attributed to the lines typical of BEA framework topology of both samples and more importantly, the shoulder peak located at ~43.4° is corresponding to the Cu phase [90]. Moreover, the Scherer equation was also used to calculate the average particle size of Ni phase and the corresponding results are presented in Table 2. The data achieved with Scherer equation is in significant agreement with the TEM results (Table 3).

Moreover, the infrared spectrum of AC support (Fig. 9B), showed the characteristic bands at 3426, 2932, 1648, 1430, 1372 and the zone of 610–1000 cm⁻¹ which correspond to O–H stretching of alcohol, C–H stretching of alkanes, C=O stretching of aliphatic ketone, C–H stretching of methyl group, C=C stretching of conjugated alkene, aromatic C–C stretching, O–H bending of carboxylic acids, C–O stretching of alcohol, C–O stretching of aliphatic ether, S=O stretching of sulfonate and =C–H bending of alkene [91]. They significantly confirm the existence of oxygen functional groups on its surface without any pre- or post-treatments. Thus this desired property avoids the further oxidation procedure necessary to enhance the surface structure of the catalyst support and makes AC a suitable material for such applications.

As it was demonstrated in Figure S.4., the adsorption-desorption isotherm of Ni-Cu/AC catalyst with the H-1 type hysteresis loop took place within a P/P₀ range of 0.75–0.90. This phenomenon is due to the evaporation in mesopores and capillary condensation in the mesopores that resulted in the corresponding PSD of Ni-Cu/AC sample in a range of 0.5–2.5 nm [92]. The mentioned condensation procedure also resulted in the shifts of the isotherms to the lower P/P₀ values compared with pure GNS sample, that proved the occupation of GNS support pores by Ni and Ru, Co, and Cu that is in the perfect agreement with the S_{BET} results. Notably, High S_{BET} and mesoporous structure makes the

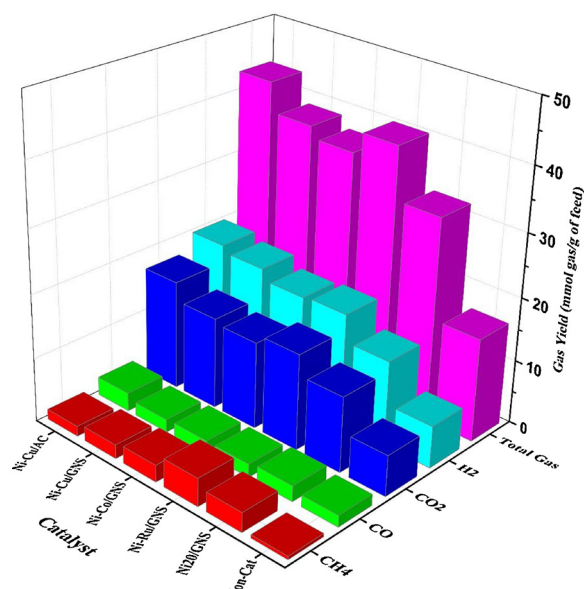


Fig. 8. Individual and total gas yields obtained from the HTG process in the presence of Ni20/GNS, Ni-Ru/GNS, Ni-Co/GNS, Ni-Cu/GNS, and Ni-Cu/AC catalysts.

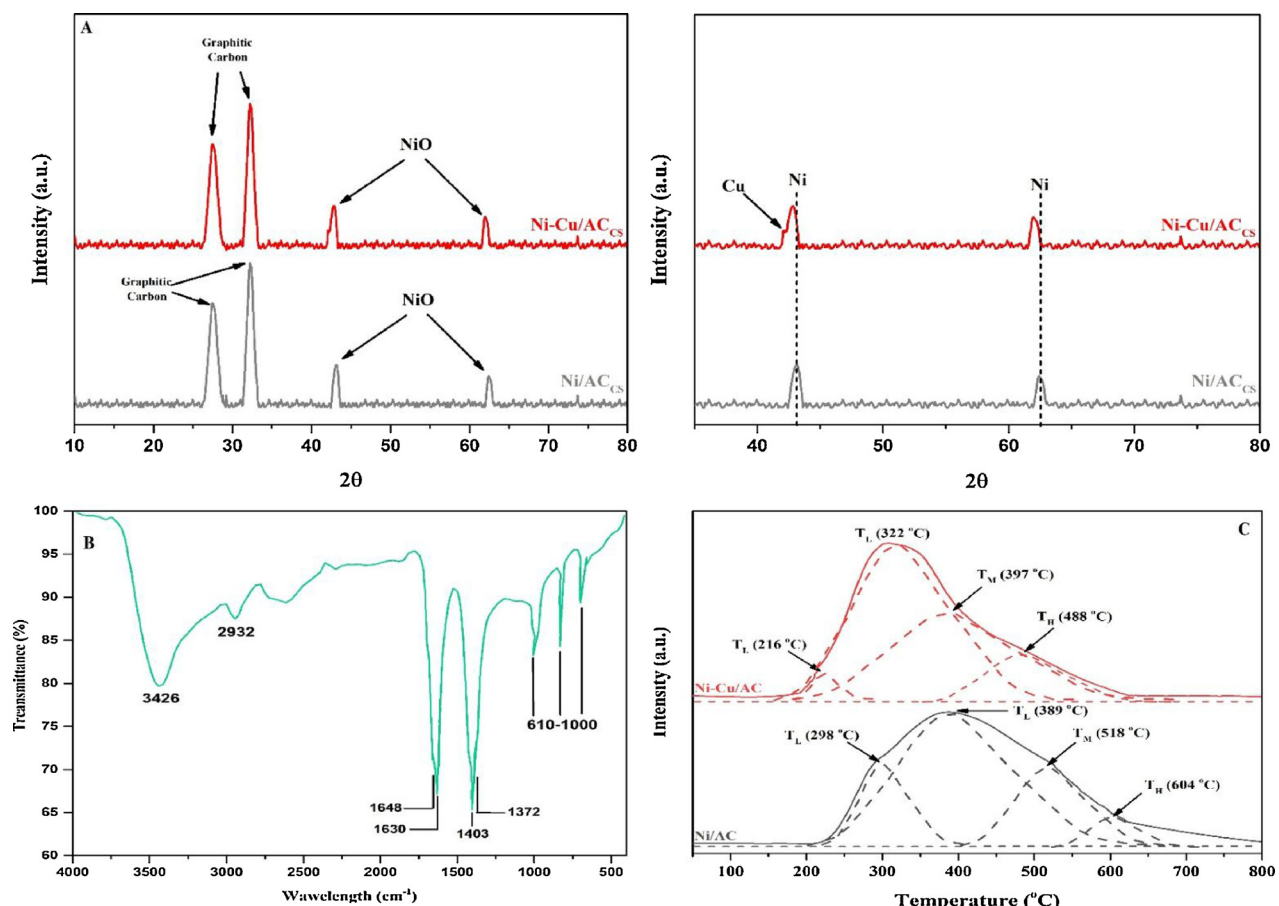


Fig. 9. ACcs supported catalyst surface Morphology and chemistry analyses results; A) XRD, B) FT-IR, and C) H₂-TPR.

diffusivity of the reactants into the active metallic sites more feasible and promotes the catalytic activity [93]. Table 3 compares the BET surface area, pore volume and average pore size of the catalyst supports (GNS and AC), synthesized mesoporous and co-impregnated catalysts used in this project.

As the isotherms suggested, the GNS supported samples displayed a much larger proportion of mesopores than the AC supported one. However, the Ni-Cu/AC sample has a larger Micropore volume. The higher decrease in the S_{BET} of AC compared to GNS is due to the more pronounced blockage of the pores by the addition of Ni particles [94]. Thus it can be concluded that GNS supported catalysts have larger straight graphitic planes, while the AC supported samples contain more amorphous carbon [95]. On the other hand, data in Table 3 proves previously reported observations that is a continuous decrease of the BET surface area for the co-impregnated GNS supported samples [96,97]. In any case, the decrease of the both micro- and mesoporous volumes for AC and GNS is indicative of a successful dispersion of Ni and (Ru, Co, and Cu) on the designated catalyst supports. AC support has a high surface area (474 m²/g), which was decreased by the loading of metallic Ni and Cu in the Ni-Cu/AC catalyst. The high BET surface area of GNS that was 602 m²/g with the pore volume of 0.66 cm³/g obviously reduced by ~50% and ~40% respectively, after the co-impregnation step. The variation in the S_{BET} of monometallic GNS supported Ni catalysts (Ni10/GNS, Ni15/GNS, Ni20/GNS, Ni30/GNS) catalysts could be related to the i) variation in mass density of the mentioned catalysts, ii) the different amount of Ni and Ru, Co, and Cu coatings of the GNS surface, iii) and the different amount of interactions between GNS and metal particles [98]. In brief, compared with the GNS supported catalysts, the Ni-Cu/AC catalyst showed low specific surface area, pore volume, and average pore size due to the much more growing up of several aggregates of NiO particles and more plugging of

its micropores [99]. This observation proves the good hydrothermal stability of this catalyst.

The H₂-TPR profiles for the as-deposited mono- and bimetallic Ni/AC and Ni-Cu/AC catalysts are shown in Fig. 9C before their H₂ reduction. According to the reduction pattern of Ni (20%)/AC sample, only one broad reduction behavior at ~220–680 °C was clearly observed which is not only attributed to the reduction of bulk NiO on the outer surface of the AC but also the existence of different degrees of metal – support interactions [90]. After deconvolution, the reduction peaks at 298, 389, 518, and 604 °C were unfolded which each one corresponds to the reduction of pure NiO to metallic Ni, strong interaction between the Ni species and the support, and the reduction of Ni²⁺ in hexagonal prisms [100], respectively. On the contrary, the corresponding reduction peak of Ni-Cu/AC catalyst, the whole broad reduction peak shifted to lower temperatures. The observed phenomenon may be explained by the hydrogen spillover that was caused by the Cu particles which lead to the faster nucleation of Ni thus improved the reducibility of NiO species at relatively low temperatures [101,102]. On the other hand, comparing the H₂ consumption amount of TPR peak for Ni-Cu/AC and Ni/AC samples, the former clearly showed the larger TPR peak at 322 °C, suggesting the impact of Cu particles in increasing the active sites and the reducibility. Other factors which decreased the reduction temperature of the Ni-Cu/AC catalyst might be attributed to the more bulk NiO species content, developed interaction between Ni and Cu particles and significant dispersion of Ni and Cu metal nanoparticles, all of which are in perfect agreement with the XRD results.

The main reduction peak and a broad reduction peak beside a weak one were observed for Ni-Cu/AC centered at 216 °C, 322 °C and 397 °C respectively corresponding to the two-step reduction of CuO to Cu₂O and CuO, and NiO reduction to metallic Ni sites [103]. Moreover, a

single reduction peak with a maximum temperature centered at 488 °C was also observed which is attributed to the reduction behavior of monometallic samples [104], thus indicating the close interaction of Ni and Cu particles which proves the successful formation of bimetallic Ni-Cu nanoparticles.

Furthermore, Fig. 10 indicates the presence of homogenously distributed Ni and/or NiO nanoparticles with no distinguishable Ni aggregation due to the more organized and controlled mesoporosity of the prepared AC support. The nanoparticles had a mean particle size of 12.3 nm. Furthermore, it is important to point out that it was not possible to distinguish between Cu and Ni in the AC supported catalyst, as both species appear in the images as black dots due to their similar electron density which resulted in their similar black dot appearance [105].

In order to demonstrate the changes in the morphological structure and physical properties of CS and AC, as an indicative of the successful catalyst support preparation, their surface morphology was revealed by the FESEM analyses and results are shown in Fig. 10. According to this figure, a common cellular structure of lignocellulosic biomass with a rough surface is observable in the FESEM image of CS [106]. As revealed in this figure, KOH activation of CS resulted in a major morphological transformation between the former and AC. These transformations suggest the appropriate enhancement of the catalyst support including the formation of a well-developed surface with larger individual grains and formation of more orderly pores [107].

On the basis of TOF results (Figure S.5.), the influence of support is more significant in the case of Ni-Cu/AC versus Ni-Co/GNS and Ni-Cu/GNS catalysts, with a difference of about 15 (s^{-1}), while Ru promoted catalysts (Ni-Ru/GNS) showed 60.92 (s^{-1}) of TOF that is very similar to Ni-Cu/AC. This similarity is originated from the TOF calculation where CGE was used for this purpose. In another word, the TOF parameter reveals the capability of the catalytic sites in feed conversion to gaseous products, thus Ru can enhance gas production over individual Ni sites on the GNS support as was discussed previously in this work. In order to overcome the present misunderstanding, the H₂ selectivity was also utilized alongside with TOF results. As it can be seen, Ni-Cu/AC catalyst shows much better performance in H₂ selectivity rather than Ni-Ru/GNS catalyst despite their similarity in TOF values. This result suggests that the individual catalytic sites on the surface of Ni-Cu/AC catalyst sample show much better performance toward CS conversion to our desired gaseous product (H₂ Gas). Represented data in Table S.1. reveal that the superiority of Ni-Cu/AC catalyst not only originates from the higher activity in individual active sites, but also it is mainly attributed to the dispersion and the total number of the aforementioned active sites on the surface of AC. The higher dispersion of catalytic sites on the surface of AC compared to GNS supported catalysts is likely related to the surface chemistry of the support. As it was mentioned earlier (FT-IR results), the more oxygenated groups on the surface of the support lead to the better dispersion of the active sites. Moreover, the better dispersion of catalytic sites would consequently result in an increase in the number of these sites on the surface of the AC with

reduced crystallite sizes [108]. The data reported in the TEM, XRD, H₂-TPR and H₂-Chemisorption results (Tables 5 and S.1.) thoroughly confirm this observation. The total amount of H₂ consumption obtained from TPR peaks was presented in Table S.1. where the AC supported catalysts show significantly larger H₂ uptake in comparison to GNS supported samples. The lower reduction temperature and the higher H₂ consumption of the Ni-Cu/AC sample compared to the Ni/AC catalyst may be attributed to the more bulk NiO contents and higher dispersion of metal nanoparticles on its surface, which was previously confirmed by XRD analysis. In conclusion, the better overall catalytic activity of the Ni-Cu/AC catalyst may be attributed to all the discussed factors such as the higher H₂ consumption, higher Ni dispersion, and the lower nanoparticle size which resulted in higher number of catalytic active sites for the AC supported catalyst compared to GNS supported ones (Table S.1.) [109].

In point of fact, Cu particles impregnated on the AC were more capable of promoting the activity of the Ni active sites especially on the AC support (in accordance with BET results, Table 3) and thus the yields of the total and individual (CO, CO₂, and H₂) gaseous products were much superior due to the enhancement of the overall and steam reforming reactions (Eqs. (6) and (7)). Further investigations also proved the impact of Cu sites on the reduction of CH₄ formation due to its intrinsic ability in preventing the methanation reaction (Eq. (10)) [110], which has lead to the significant conversion of methane to its gaseous precursors and once again demonstrated its superior performance while being impregnated on the AC support compared to GNS [111]. According to the previous results discussed in this project, higher production of H₂, CO₂ and CO yields is due to the enhanced surface morphology and chemistry besides the higher metal dispersion of Ni-Cu/AC catalyst compared to the GNS supported ones. These results proved that AC as catalyst support can disperse both Ni and Cu particles homogeneously and uniformly on its mesoporous structure [110]. In conclusion, the cost-effective Ni-Cu/AC bimetallic catalysts showed the highest potential to replace the expensive GNS supported catalyst in CHTG process for H₂-rich gas production [112].

4. Conclusion

The work herein provides the advantages of Ni (20%)/AC, and Ni (20%) – Cu (2%)/AC catalysts over the conventional bimetallic Ni/GNS catalysts in the HTG of lignocellulosic biomass (CS) performed in a stainless-steel batch reactor under SCW for the highest possible H₂ gas production. We have investigated the most significant control factors such as temperature, reaction time, and feed concentration in the absence of catalysts to firstly optimize the impact of the operational parameters on the H₂ gas yield, concluding that temperature had the highest impact on the process, while reaction time and feed concentration were of less importance. Secondly the performance and properties of different binary metal catalysts supported on GNS using Ni and different noble metals (Ru, Co, and Cu) as promoters were investigated using various analyses such as XRD, H₂-TPR, and FESEM,

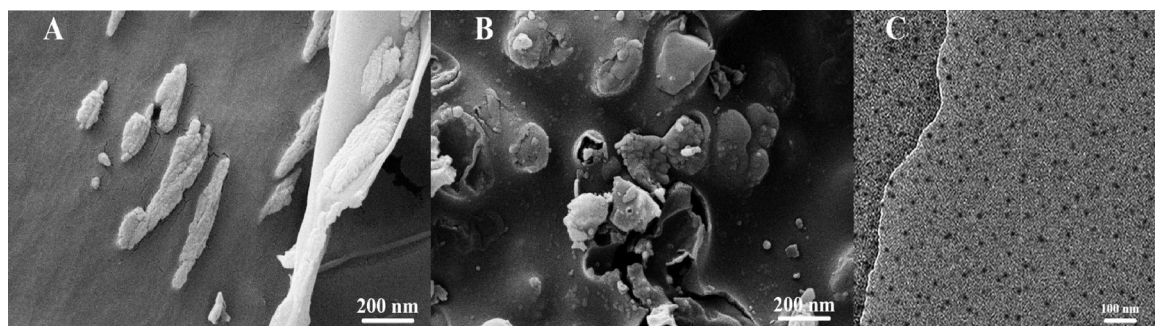


Fig. 10. FESEM images of A) CS, and B) AC C) TEM images Fresh calcined 20 wt% Ni-Cu/AC.

proving the ability of Ni/GNS catalysts in enhancing the H₂ and methane production due to cleavage of the C–C bonds in the biomass structure and suggesting the successful dispersion of metal species on the utilized catalyst supports. The addition of Ru, Co, and Cu to Ni-based catalysts also enhanced the H₂ gas yield by accelerating the reforming reaction. Thirdly, investigation of the catalyst properties through a variety of characterization techniques suggested copper as the optimum promoter due to its high ability in the promotion of the WGS reaction. Decelerating methanation reaction, promoting the reforming of methane, and producing the highest yield of H₂ gas are among the major benefits of using Cu as promoter. Thus, Ni (20%)/AC, and Ni (20%) – Cu (2%)/AC catalysts were prepared and utilized in the optimized HTG process. The mentioned catalyst resulted in further improvement over the process and showed higher activity, excellent catalytic performance, and stability. Finally, we conclude that the higher production of H₂, CO₂ and CO yields are due to the enhanced surface morphology and chemistry besides the higher metal dispersion of AC supported catalysts compared to the GNS supported ones.

Author contributions

M.S and S.B conceived the idea, designed the experiments, performed the operations and co-wrote the Manuscript. H.H and KK collected and analyzed data, and helped finish the experiments. A.T commented on and improved the manuscript. All authors discussed the results.

Acknowledgments

The authors would like to acknowledge “the Research Institute of Petroleum Industry” and “The catalyst and chemical reactions laboratory” at the University of Tehran beside our fellow colleagues that provided us the opportunity to finish the project.

Appendix A. Supplementary data

Supplementary material related to this article can be found, in the online version, at doi:<https://doi.org/10.1016/j.apcatb.2018.08.039>.

References

- [1] J.W. Han, J.S. Park, M.S. Choi, H. Lee, Uncoupling the size and support effects of Ni catalysts for dry reforming of methane, *Appl. Catal. B Environ.* 203 (2017) 625–632, <https://doi.org/10.1016/J.APCATB.2016.10.069>.
- [2] P.M. Mortensen, J.-D. Grunwaldt, P.A. Jensen, K.G. Knudsen, A.D. Jensen, A review of catalytic upgrading of bio-oil to engine fuels, *Appl. Catal. A Gen.* 407 (2011) 1–19, <https://doi.org/10.1016/J.APCATA.2011.08.046>.
- [3] R.D. Cortright, R.R. Davda, J.A. Dumesic, Hydrogen from catalytic reforming of biomass-derived hydrocarbons in liquid water, *Nature* 418 (2002) 964, <https://doi.org/10.1038/nature01009>.
- [4] G.W. Huber, S. Iborra, A. Corma, Synthesis of transportation fuels from biomass: chemistry, catalysts, and engineering, *Chem. Rev.* 106 (2006) 4044–4098, <https://doi.org/10.1021/cr068360d>.
- [5] A. Corma, S. Iborra, A. Velty, Chemical routes for the transformation of biomass into chemicals, *Chem. Rev.* 107 (2007) 2411–2502, <https://doi.org/10.1021/cr050989d>.
- [6] C. Liu, H. Wang, A.M. Karim, J. Sun, Y. Wang, Catalytic fast pyrolysis of lignocellulosic biomass, *Chem. Soc. Rev.* 43 (2014) 7594–7623, <https://doi.org/10.1039/C3CS60414D>.
- [7] Q. Chen, R. Yang, B. Zhao, Y. Li, S. Wang, H. Wu, Y. Zhuo, C. Chen, Investigation of heat of biomass pyrolysis and secondary reactions by simultaneous thermogravimetry and differential scanning calorimetry, *Fuel* 134 (2014) 467–476, <https://doi.org/10.1016/j.fuel.2014.05.092>.
- [8] M.S.H.K. Tushar, A. Dutta, C.(Charles) Xu, Catalytic supercritical gasification of biocrude from hydrothermal liquefaction of cattle manure, *Appl. Catal. B Environ.* 189 (2016) 119–132, <https://doi.org/10.1016/j.apcatb.2016.02.032>.
- [9] A. Arregi, M. Amutio, G. Lopez, J. Bilbao, M. Olazar, Evaluation of thermochemical routes for hydrogen production from biomass: a review, *Energy Convers. Manag.* 165 (2018) 696–719, <https://doi.org/10.1016/j.enconman.2018.03.089>.
- [10] D.B. Levin, R. Chahine, Challenges for renewable hydrogen production from biomass, *Int. J. Hydrogen Energy* 35 (2010) 4962–4969, <https://doi.org/10.1016/j.ijhydene.2009.08.067>.
- [11] C. Li, X. Zhao, A. Wang, G.W. Huber, T. Zhang, Catalytic transformation of lignin for the production of chemicals and fuels, *Chem. Rev.* 115 (2015) 11559–11624, <https://doi.org/10.1021/acs.chemrev.5b00155>.
- [12] D.A. Cantero, C. Martinez, M.D. Bermejo, M.J. Cocero, Simultaneous and selective recovery of cellulose and hemicellulose fractions from wheat bran by supercritical water hydrolysis, *Green Chem.* 17 (2015) 610–618, <https://doi.org/10.1039/C4GC01359J>.
- [13] M. Salimi, B. Nejati, A. Karimi, A. Tavasoli, Hydrothermal gasification performance of iranian rice straw in supercritical water media for hydrogen-rich gas production, *BioResources* 11 (2016) 6362–6377, <https://doi.org/10.1537/biores.11.3.6362-6377>.
- [14] P. Cheali, K.V. Gernaey, G. Sin, Toward a computer-aided synthesis and design of biorefinery networks: data collection and management using a generic modeling approach, *ACS Sustain. Chem. Eng.* 2 (2014) 19–29, <https://doi.org/10.1021/sc400179f>.
- [15] P. Zhao, Y. Shen, S. Ge, Z. Chen, K. Yoshikawa, Clean solid biofuel production from high moisture content waste biomass employing hydrothermal treatment, *Appl. Energy* 131 (2014) 345–367, <https://doi.org/10.1016/j.apenergy.2014.06.038>.
- [16] A. Tayyebi, O. Akhavan, B.-K. Lee, M. Outokehsh, Supercritical water in top-down formation of tunable-sized graphene quantum dots applicable in effective photo-thermal treatments of tissues, *Carbon* 130 (2018) 267–272, <https://doi.org/10.1016/j.carbon.2017.12.057>.
- [17] K. Kang, R. Azargohar, A.K. Dalai, H. Wang, Hydrogen production from lignin, cellulose and waste biomass via supercritical water gasification: catalyst activity and process optimization study, *Energy Convers. Manag.* 117 (2016) 528–537, <https://doi.org/10.1016/j.enconman.2016.03.008>.
- [18] L.J. Guo, Y.J. Lu, X.M. Zhang, C.M. Ji, Y. Guan, A.X. Pei, Hydrogen production by biomass gasification in supercritical water: a systematic experimental and analytical study, *Catal. Today* 129 (2007) 275–286, <https://doi.org/10.1016/j.cattod.2007.05.027>.
- [19] Y. Guo, S. Wang, C.M. Huelsman, P.E. Savage, Kinetic model for reactions of indole under supercritical water gasification conditions, *Chem. Eng. J.* 241 (2014) 327–335, <https://doi.org/10.1016/j.cej.2013.11.012>.
- [20] G. Garbarino, C. Wang, I. Valsamakis, S. Chitsazan, P. Riani, E. Finocchio, M. Flytzani-Stephanopoulos, G. Busca, A study of Ni/Al₂O₃ and Ni-La/Al₂O₃ catalysts for the steam reforming of ethanol and phenol, *Appl. Catal. B Environ.* 174–175 (2015) 21–34, <https://doi.org/10.1016/j.apcatb.2015.02.024>.
- [21] W.-J. Liu, W.-W. Li, H. Jiang, H.-Q. Yu, Fates of chemical elements in biomass during its pyrolysis, *Chem. Rev.* 117 (2017) 6367–6398, <https://doi.org/10.1021/acs.chemrev.6b00647>.
- [22] A. May, J. Salvadó, C. Torras, D. Montané, Catalytic gasification of glycerol in supercritical water, *Chem. Eng. J.* 160 (2010) 751–759, <https://doi.org/10.1016/j.cej.2010.04.005>.
- [23] H. Kobayashi, T. Komanoya, S.K. Guha, K. Hara, A. Fukuoka, Conversion of cellulose into renewable chemicals by supported metal catalysis, *Appl. Catal. A Gen.* 409–410 (2011) 13–20, <https://doi.org/10.1016/j.apcata.2011.10.014>.
- [24] R. Muangrat, J.A. Onwudili, P.T. Williams, Influence of alkali catalysts on the production of hydrogen-rich gas from the hydrothermal gasification of food processing waste, *Appl. Catal. B Environ.* 100 (2010) 440–449, <https://doi.org/10.1016/j.apcatb.2010.08.019>.
- [25] D.M. Alonso, J.Q. Bond, J.A. Dumesic, Catalytic conversion of biomass to biofuels, *Green Chem.* 12 (2010) 1493–1513, <https://doi.org/10.1039/C004654J>.
- [26] M. Sankar, N. Dimitratos, P.J. Miedziak, P.P. Wells, C.J. Kiely, G.J. Hutchings, Designing bimetallic catalysts for a green and sustainable future, *Chem. Soc. Rev.* 41 (2012) 8099–8139, <https://doi.org/10.1039/C2CS35296F>.
- [27] G. Özkan, S. Gök, G. Özkan, Active carbon-supported Ni, Ni/Cu and Ni/Cu/Pd catalyzed steam reforming of ethanol for the production of hydrogen, *Chem. Eng. J.* 171 (2011) 1270–1275, <https://doi.org/10.1016/j.cej.2011.05.051>.
- [28] J.N. Jocz, L.T. Thompson, P.E. Savage, Catalyst oxidation and dissolution in supercritical water, *Chem. Mater.* 30 (2018) 1218–1229, <https://doi.org/10.1021/acs.chemmater.7b03713>.
- [29] C. Wu, L. Wang, P.T. Williams, J. Shi, J. Huang, Hydrogen production from biomass gasification with Ni/MCM-41 catalysts: influence of Ni content, *Appl. Catal. B Environ.* 108–109 (2011) 6–13, <https://doi.org/10.1016/j.apcatb.2011.07.023>.
- [30] E. González, C. Marchant, C. Sepúlveda, R. García, I.T. Ghompson, N. Escalona, J.L. García-Fierro, Hydrogenation of sodium hydrogen carbonate in aqueous phase using metal/activated carbon catalysts, *Appl. Catal. B Environ.* 224 (2018) 368–375, <https://doi.org/10.1016/j.apcatb.2017.10.038>.
- [31] A. Kubacka, M. Fernández-García, A. Martínez-Arias, Catalytic hydrogen production through WGS or steam reforming of alcohols over Cu, Ni and Co catalysts, *Appl. Catal. A Gen.* 518 (2016) 2–17, <https://doi.org/10.1016/j.apcata.2016.01.027>.
- [32] T. Sato, K. Inda, N. Itoh, Gasification of bean curd refuse with carbon supported noble metal catalysts in supercritical water, *Biomass Bioenergy* 35 (2011) 1245–1251, <https://doi.org/10.1016/j.biombioe.2010.12.015>.
- [33] C. He, J. Zheng, K. Wang, H. Lin, J.-Y. Wang, Y. Yang, Sorption enhanced aqueous phase reforming of glycerol for hydrogen production over Pt-Ni supported on multi-walled carbon nanotubes, *Appl. Catal. B Environ.* 162 (2015) 401–411, <https://doi.org/10.1016/j.apcatb.2014.07.012>.
- [34] G. Fiori, F. Bonaccorso, G. Iannaccone, T. Palacios, D. Neumaier, A. Seabaugh, S.K. Banerjee, L. Colombo, Electronics based on two-dimensional materials, *Nat. Nanotechnol.* 9 (2014) 768, <https://doi.org/10.1038/nnano.2014.207>.
- [35] C.N.R. Rao, K. Gopalakrishnan, U. Maitra, Comparative study of potential applications of graphene, MoS₂, and other two-dimensional materials in energy devices, sensors, and related areas, *ACS Appl. Mater. Interfaces* 7 (2015) 7809–7832, <https://doi.org/10.1021/am509096x>.
- [36] S.S. Varghese, S. Lonkar, K.K. Singh, S. Swaminathan, A. Abdala, Recent advances

in graphene based gas sensors, Sensors Actuators B Chem. 218 (2015) 160–183, <https://doi.org/10.1016/j.snb.2015.04.062>.

[37] H. Wang, Y. Zhang, Y. Wang, H. Ma, B. Du, Q. Wei, Facile synthesis of cuprous oxide nanowires decorated graphene oxide nanosheets nanocomposites and its application in label-free electrochemical immunosensor, Biosens. Bioelectron. 87 (2017) 745–751, <https://doi.org/10.1016/j.bios.2016.09.014>.

[38] T. Wang, P. Hu, C. Zhang, H. Du, Z. Zhang, X. Wang, S. Chen, J. Xiong, G. Cui, Nickel disulfide–Graphene nanosheets composites with improved electrochemical performance for sodium ion battery, ACS Appl. Mater. Interfaces 8 (2016) 7811–7817, <https://doi.org/10.1021/acsami.6b00179>.

[39] J.P.C. Trigueiro, R.L. Lavall, G.G. Silva, Nanocomposites of graphene Nanosheets/Multiwalled carbon nanotubes as electrodes for in-plane supercapacitors, Electrochim. Acta 187 (2016) 312–322, <https://doi.org/10.1016/j.electacta.2015.11.053>.

[40] Z. Xu, C. Gao, Graphene in macroscopic order: liquid crystals and wet-spun fibers, Acc. Chem. Res. 47 (2014) 1267–1276, <https://doi.org/10.1021/ar4002813>.

[41] W. Zhou, J. Zhou, Y. Zhou, J. Lu, K. Zhou, L. Yang, Z. Tang, L. Li, S. Chen, N-doped carbon-wrapped cobalt nanoparticles on N-Doped graphene nanosheets for high-efficiency hydrogen production, Chem. Mater. 27 (2015) 2026–2032, <https://doi.org/10.1021/acs.chemmater.5b00331>.

[42] K. He, G. Chen, G. Zeng, A. Chen, Z. Huang, J. Shi, T. Huang, M. Peng, L. Hu, Three-dimensional graphene supported catalysts for organic dyes degradation, Appl. Catal. B Environ. 228 (2018) 19–28, <https://doi.org/10.1016/j.apcatb.2018.01.061>.

[43] R. Shi, J. Zhao, S. Liu, W. Sun, H. Li, P. Hao, Z. Li, J. Ren, Nitrogen-doped graphene supported copper catalysts for methanol oxidative carbonylation: enhancement of catalytic activity and stability by nitrogen species, Carbon N. Y. 130 (2018) 185–195, <https://doi.org/10.1016/j.carbon.2018.01.011>.

[44] M. Inagaki, M. Toyoda, Y. Soneda, T. Morishita, Nitrogen-doped carbon materials, Carbon N. Y. 132 (2018) 104–140, <https://doi.org/10.1016/j.carbon.2018.02.024>.

[45] N. Ding, R. Azargohar, A.K. Dalai, J.A. Kozinski, Catalytic gasification of glucose to H₂ in supercritical water, Fuel Process. Technol. 127 (2014) 33–40, <https://doi.org/10.1016/j.fuproc.2014.05.014>.

[46] P.R. Shukla, S. Wang, H. Sun, H.M. Ang, M. Tadé, Activated carbon supported cobalt catalysts for advanced oxidation of organic contaminants in aqueous solution, Appl. Catal. B Environ. 100 (2010) 529–534, <https://doi.org/10.1016/j.apcatb.2010.09.006>.

[47] G. Peng, C. Ludwig, F. Vogel, Catalytic supercritical water gasification: interaction of sulfur with ZnO and the ruthenium catalyst, Appl. Catal. B Environ. 202 (2017) 262–268, <https://doi.org/10.1016/j.apcatb.2016.09.011>.

[48] M. Salimi, S. Balou, K. Kohansal, K. Babaei, A. Tavasoli, M. Andache, Optimizing the preparation of meso- and microporous canola stalk-derived hydrothermal carbon via response surface methodology for methylene blue removal, Energy Fuels 31 (2017) 12327–12338, <https://doi.org/10.1021/acs.energyfuels.7b02440>.

[49] G. Wang, X. Shen, B. Wang, J. Yao, J. Park, Synthesis and characterisation of hydrophilic and organophilic graphene nanosheets, Carbon N. Y. 47 (2009) 1359–1364, <https://doi.org/10.1016/j.carbon.2009.01.027>.

[50] H. Ay, D. Üner, Dry reforming of methane over CeO₂ supported Ni, Co and Ni–Co catalysts, Appl. Catal. B Environ. 179 (2015) 128–138, <https://doi.org/10.1016/j.apcatb.2015.05.013>.